University of Pisa

Laboratory Report

Analysis of the Coalescence of Binary Black Hole GW170814 with LIGO and Virgo, and SGWB Analysis with the Einstein Telescope

Professors:
Prof. Massimiliano Razzano
Prof. Angelo Ricciardone
Prof. Barbara Patricelli
Prof. Andrea Pallottini

Candidates:
Nicolò Aimone Braida (701844)
Matilde Biscaro (702943)
Lorenzo Nepi (701845)

Academic Year: 2024-2025

April. 2025

Abstract

On August 14, 2017, the LIGO and Virgo interferometers observed a gravitational-wave signal originating from the merger of two stellar-mass black holes. We found that the signal was first detected at LIGO Livingston, followed by Hanford and Virgo with delays of approximately 9 ms and 13 ms, respectively. The signal analysis yielded SNR values of approximately ∼8.8 for the Hanford detector, ∼11.8 for Livingston, and ∼3.6 for Virgo. The estimated component masses of the two black holes were $(m_1, m_2) = (31.6 \pm 0.4, 28.4 \pm 0.4)\, M_\odot$ for Hanford, $(32.4 \pm 0.4, 28.4 \pm 0.4)\, M_\odot$ for Livingston, and $(36.4 \pm 0.4, 29.4 \pm 0.4)\, M_\odot$ for Virgo.
Finally, a simulated Stochastic Gravitational Wave Background (SGWB) signal was analyzed by estimating the SNR that the Einstein Telescope in its two-arm configuration (ET2L) would achieve. The SNR values obtained from the simulated data are 26.4 for the aligned setup and 0.52 for the misaligned setup.

Contents

1 Introduction 1
- 1.1 Gravitational Waves from a binary system 1
- 1.2 LIGO-Virgo-KAGRA . . . 2
- 1.3 Noise and SNR . . . 2
- 1.4 Observational horizon of the detectors . . 3
- 1.5 The signal . . . 3

2 Analysis 3
- 2.1 Detector noise analysis and ASD . . . 4
- 2.2 Cleaning data and time domain analysis . 4
- 2.3 Optimal detection filter . . . 4

3 SGWB 4
- 3.1 Einstein Telescope . . . 5
- 3.2 SNR estimation for ET2L . . . 5
  - 3.2.1 Theoretical SNR . . . 5
  - 3.2.2 SNR from simulated data . . . 6

4 Results 6
- 4.1 GW170814 . . . 6
- 4.2 SGWB . . . 9

5 Discussion 9
- 5.1 GW170814 . . . 9
- 5.2 SGWB . . . 10

6 Conclusion 10

A Appendix 10
- A.1 Cholesky matrix . . . 10

References 11

1 Introduction

Gravitational waves (GWs), first predicted by Einstein in 1916 inside the linearized General Relativity framework, represent perturbations in the fabric of spacetime generated by accelerated massive bodies. Among the most promising and well-studied GW sources are coalescing binary systems composed of compact objects, such as black holes (BHs) and neutron stars (NSs). The detection of gravitational waves from such systems has become a routine capability of the current global network of ground-based interferometric detectors. Operating in the frequency band $\sim 10^1 - 10^4$ Hz, Advanced LIGO (H1 and L1), Advanced Virgo (V1), and KAGRA constitute the primary instruments for observing transient GW signals originating from binary black hole (BBH), binary neutron star (BNS), and neutron star–black hole (NS–BH) mergers.

This work presents a detailed analysis of the event GW170814, a coalescence of two stellar mass black holes observed during the O2 run by the LIGO–Virgo detector network on August 14, 2017 at 10:30:43 UTC. The signal is analyzed in both the time and frequency domains, with a focus on the application of matched filtering algorithms for signal recovery and mass estimation.

1.1 Gravitational Waves from a binary system

A binary system composed of two compact objects in orbit emits gravitational waves due to the acceleration of the masses. In the *early inspiral* phase, where the gravitational field is weak and the velocities are non-relativistic, the system can be accurately described using the quadrupole approximation. The amplitude of the two polarization of a gravitational waves observed at a distance r, in *far-field* approximations, is given by

$$\begin{aligned} h_+(t_{ret}) &\sim \frac{4G\mu a^2\omega^2}{c^4 r}\cos(2\omega t_{ret})\,, \\ h_\times(t_{ret}) &\sim \frac{4G\mu a^2\omega^2}{c^4 r}\sin(2\omega t_{ret})\,, \end{aligned} \tag{1}$$

where μ is the reduced mass, a is the semi-major axis, ω is the orbital frequency, and t_{ret} is the retarded time. The power L_{GW} radiated in the form of gravitational waves is

given by

$$L_{\rm GW} = \frac{32}{5}\frac{G^4}{c^5}\frac{(m_1 m_2)^2(m_1+m_2)}{a^5}\,. \qquad (2)$$

As the system loses energy, the orbital separation decreases, leading to an increase in both the wave frequency and amplitude, which results in a characteristic "chirp" signal. The process ends with the *merger* of the two bodies, followed by a *ringdown phase* during which the final object settles into a stable configuration.
A key quantity in this process is the chirp mass M_c, which determines how the gravitational wave frequency changes over time

$$\dot{f}_{GW} = \frac{96}{5}\pi^{8/3}\left(\frac{GM_c}{c^3}\right)^{5/3} f_{GW}^{11/3}\,. \qquad (3)$$

The temporal evolution of the frequency and phase of the signal is essential for source identification and for extracting astrophysical parameters from gravitational wave observations.

1.2 LIGO-Virgo-KAGRA

Ground-based gravitational wave detectors such as LIGO and Virgo operate as dual-arm laser interferometers, designed to measure differential length changes induced by the passage of a gravitational wave. In its simplest configuration, the interferometer follows a Michelson layout, where a laser beam is split into two orthogonal arms by a beam splitter, reflected by two mirrors, and recombined to produce an interference pattern on a photodetector. Fluctuations in arm lengths $\Delta L = L_x - L_y$ induced by the GW strain $h(t)$ produce a measurable variation in output intensity. In the absence of perturbations, the arms are adjusted to operate near destructive interference (*dark fringe*) to reduce optical noise from the laser.
The theoretical sensitivity of such a system is optimized when the arm length L satisfies $\tilde{L} = \lambda_G/4$, where λ_G is the GW wavelength. For GW frequencies around 100 Hz, this condition corresponds to $\tilde{L} \sim 750$ km, a length scale that is unreachable for a terrestrial interferometer. To overcome this limitation, modern interferometers implement Fabry-Perot cavities within each arm, effectively increasing the optical path length through multiple reflections on secondary mirrors. Additional components such as power- and signal-recycling mirrors further enhance the circulating power and frequency response, while mode cleaners suppress optical noise. A schematic representation of the interferometer is reported in Fig. 1. The resulting architecture is a dual-recycled Fabry-Perot Michelson interferometer. Modern instruments are capable of detecting strain amplitudes as small as $h \sim 10^{-23}$, corresponding to length displacements in the order of 10^{-19} m. Achieving such sensitivity requires not only a sophisticated optical design but also an extreme isolation from seismic, thermal, and quantum noise sources.
The current network of terrestrial gravitational wave detectors is composed of the two Advanced LIGO interferometers located in Hanford (H1) and Livingston (L1), the Advanced Virgo detector in Italy (V1), and the KAGRA observatory in Japan. LIGO and Virgo, both upgraded from their initial configurations (operational since

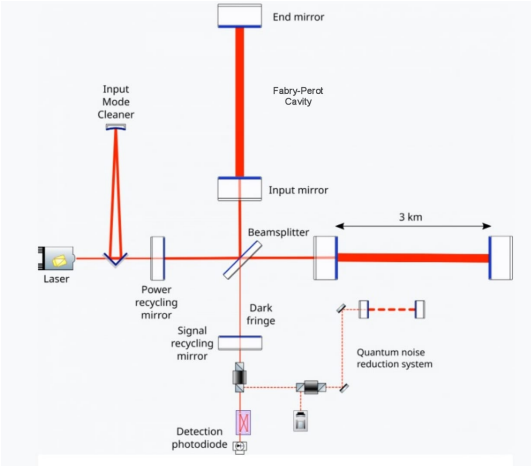

Figure 1: Schematic representation of the optical configuration of Advanced Virgo.

2002 and 2007 respectively), began joint science operations in the mid-2010s, with the landmark detection of GW150914 in 2015 marking the first direct observation of a gravitational wave signal. KAGRA, constructed underground and incorporating cryogenic technologies, joined the network in 2020 and began observational runs in 2023. The collaboration enables coincident detections across geographically separated sites, improving source localization, waveform reconstruction, and parameter estimation accuracy. The European Gravitational Observatory (EGO) coordinates the Virgo project, with broad international participation under the LIGO–Virgo–KAGRA (LVK) framework.

1.3 Noise and SNR

The main noise sources affecting this class of detectors are summarized below.

- *Photon shot noise*:
  Due to the quantum uncertainty in the emission and detection of light quanta, there are fluctuations in the intensity of the incident light beam. This is the dominant noise source at frequencies above 100 Hz.

- *Radiation pressure noise*:
  Photons striking the mirrors transfer momentum, which is itself subject to quantum uncertainty. This results in random "kicks" to the mirrors, causing fluctuations in their position. This effect mostly impacts the detector at frequencies below 100 Hz. Shot noise and radiation pressure noise are often collectively referred to as *quantum noise* and set a fundamental sensitivity limit for the detector known as *Standard Quantum Limit* (SQL).

- *Seismic noise*:
  Ground vibrations are 10-11 orders of magnitude stronger than the expected GW signals. Virgo uses a complex suspension system to isolate the mirrors, while LIGO employs active damping systems. Both detectors include arrays of sensors for local seismic monitoring. Third-generation detectors like ET will be built underground, as seismic vibrations decay exponentially with depth. Currently, seismic noise makes ground-based detections practically impossible below 1-2 Hz.

- *Thermal noise*:
  The mirrors and their suspension systems are subject to internal vibrational modes due to thermal agitation. Thermal noise also affects the beam splitter, which is traversed thousands of times by the laser light.

- *Newtonian noise*:
  Gravitational attraction between the mirrors and nearby moving masses can induce oscillations. In particular, seismic waves cause density fluctuations in the Earth's layers that act strongly on the mirrors.

To simplify the computations, while calculating the SNR for GW170814 we consider the analytical expressions typically employed for two objects during the early inspiral phase. We also assumed that the signal $S(t)$ can be decomposed in two separete components, the noise $n(t)$ and the GW signal (strain) $h(t)$.

We need to employ an appropriate filtering function $w(t)$:

$$w(t) = \int_{-\infty}^{+\infty} K(t-t')\, h(t')\, dt' \,, \tag{4}$$

where $K(t-t')$ is referred to as the *kernel*, and $h(t)$ is the signal to be filtered. This leads to a slightly different definition of the signal-to-noise ratio:

$$\left(\frac{S}{N}\right)(t) = \frac{\int_{-\infty}^{+\infty} K(t-t')\, h(t')\, dt'}{\sqrt{\left\langle \left| \int_{-\infty}^{+\infty} K(t-t')\, n(t')\, dt' \right|^2 \right\rangle}}. \tag{5}$$

Here, the noise N is defined as the *root mean square* of the filter output due solely to the noise component, while the signal S is the filter output due only to the signal $h(t)$. This approach assumes that the signal and noise contributions within the data can be separated, which is often non trivial in the *noise-dominated* regimes.
Since the choice of the kernel is arbitrary, one seeks the function K that maximizes the SNR. In the Fourier domain, the convolution theorem yields

$$\tilde{S}(f) = \tilde{K}(f)\tilde{h}(f) \quad . \tag{6}$$

By making suitable substitutions, one arrives at the expression for the SNR at $t = 0$:

$$\frac{S}{N} = \frac{\int_{-\infty}^{+\infty} \tilde{K}(f)\tilde{h}(f)\, df}{\int_{-\infty}^{+\infty} |\tilde{K}(f')|^2 S_n(f')\, df'}. \tag{7}$$

It is also useful to introduce the operator $(\,|\,)$, defined as the noise-weighted scalar product:

$$(h_1|h_2) = 2\int_0^{+\infty} \frac{\tilde{h}_1(f)\tilde{h}_2^*(f) + \tilde{h}_1^*(f)\tilde{h}_2(f)}{S_n(f)}\, df \quad . \tag{8}$$

Using this notation, the SNR can be rewritten as:

$$\frac{S}{N} = \frac{(S_h K|h)}{\sqrt{(S_n K|S_n K)}} \quad . \tag{9}$$

In the case of two vectors $\vec{v}$ and $\vec{w}$ of fixed length, their inner product is maximized when the vectors are parallel, so, when $\vec{v} \propto \vec{w}$. Analogously, the kernel that maximizes the signal-to-noise ratio (known as the *Wiener optimal filter*) satisfies the following equation:

$$S_n(f)\tilde{K}(f) \propto \tilde{h}(f) \quad \Rightarrow \quad \tilde{K}(f) \propto \frac{\tilde{h}(f)}{S_n(f)}. \tag{10}$$

It is shown that in the frequency domain, the optimal filter is given by the signal weighted by the noise power spectral density (PSD).

1.4 Observational horizon of the detectors

The amplitude of a gravitational wave from a binary system is inversely proportional to its luminosity distance. More generally, the farther a GW source is located, the weaker the strain signal detected. An higher signal amplitude typically leads to a higher SNR, which also depends on the detector's characteristics. For instance, increasing the arm length of an interferometer improves its strain sensitivity and thus enhances the SNR.
Once the source type and waveform are fixed, a given detector will be able to detect the signal and achieve an SNR significantly greater than one only up to a certain maximum distance. This defines the detector's *observational horizon*. The typical observational horizons of the main interferometers discussed for BBHs and BNSs correspond to $z \sim 2$ and $z \sim 0.5$ respectively (Fig. 2).

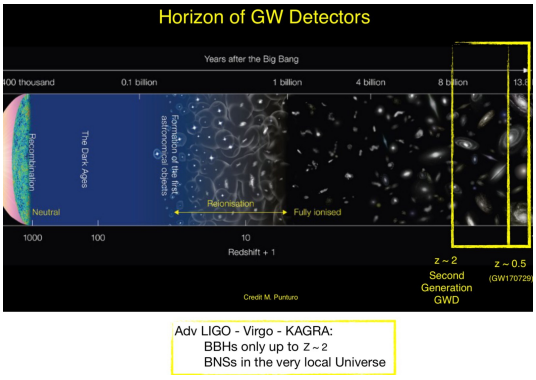

Figure 2: Representation of the observational horizon of LIGO, Virgo, KAGRA.

1.5 The signal

The event GW170814 was detected on August 14, 2017, at 10:30:43 UTC and corresponds to the merger of two binary black holes. This event marked an important point in gravitational-wave astronomy as it was the first signal observed simultaneously by three interferometers: the two LIGO detectors and Virgo. The inclusion of Virgo enabled a more precise localization of the signal's source in the sky, if compared to previous observations relying only on the two LIGO detectors [2].

2 Analysis

The data relative to GW170814 were downloaded from the Gravitational Wave Open Science Center (GWSOC) database [1]. We selected an hour time window around the event time $t_0 = 1186741861.5$ s (GPS). Then, we plotted the raw time series of the strain $h(t)$ to check if the gravitational wave signal was visible. We also plotted DataQuality-frames in order to check if the interferometers were in observing mode or not.

2.1 Detector noise analysis and ASD

Let us treat the noise as an example of a random process time series $n(t)$. It is useful to introduce the Power Spectral Density (PSD) to describe the distribution of noise through several frequencies. It is defined as the Fourier transformation of the two-point correlation function:

$$S_n(f) = \lim_{T\to\infty} \frac{1}{T} \left| \int_0^T n(t)\, e^{-i2\pi ft}\, dt \right|^2 . \qquad (11)$$

The Amplitude Spectral Density (ASD) is defined as the square root of the PSD

$$ASD(f) = \sqrt{S_n(f)}\,. \qquad (12)$$

First of all, it is necessary to build the ASD for each IFO. After plotting ASD diagram, we roughly determined if the ASD is constant in a specific frequency range in order to investigate the noise stationarity and the frequencies range in which each interferometers were most sensitive. Subsequently, we divided the selected region into 180 segments of 20 seconds each, and computed the ASD with its average and standard deviation, in order to figure out if the noise changes significantly in time.

2.2 Cleaning data and time domain analysis

We proceeded by applying a bandpass filter (50-300) Hz and a notch at 60 Hz for the LIGO interferometers to eliminate a specific power line in the ASD plot (the corresponding frequency for Virgo is 50 Hz, so it was removed by the bandpass). The bandpass is necessary in order to clean our data set and avoid frequencies out of the sensitive domain.

2.3 Optimal detection filter

Thanks to the PyCBC library, it is possible to build a signal template and adopt the *matched filtering technique*.

Matched filtering is the process of applying a filter to the observed signal $s(f)$, by computing its inner product $(s|h)$ with a template waveform $h(f)$ corresponding to the gravitational-wave signal being searched for. In practice, $h(f)$ is not known *a priori*; instead, its defining parameters must be inferred from the observations. For detectors such as LIGO and Virgo, this operation is performed by computing the output of the optimal filter over a large number of parameter combinations, corresponding to various potential sources. It can be shown that, for an optimal filter, the signal-to-noise ratio (SNR) is given by

$$\left(\frac{S}{N}\right)^2 = 4 \int_{-\infty}^{+\infty} \frac{|\tilde{h}(f)|^2}{S_n(f)}\, df\,. \qquad (13)$$

Thanks to the *template bank* provided for $h(f)$, it is possible to perform matched filtering with our signal $s(f)$, in order to find the best filter $\tilde{K}$ (Eq.10) by maximizing the SNR value. It is possible to demonstrate that by maximizing the SNR, the likelihood ration will also be maximized.

We proceeded by choosing a time interval of 20 seconds around the time event and we applied a downsampling at 2048 HZ and a highpass filter at 15 Hz to remove low frequencies affected by noise. We cropped our signal, removing two seconds of data from both the beginning and end to remove the ring artifacts. Then, we evaluated the PSD over 4 seconds data using the *Welch Method*[1] and interpolated it to match our data. After that, we limited the filter length to 1/PSD and used the PSD to filter the data in a controlled way.

By assuming the coalescence of the two objects of masses m_1 and m_2, we built up a (50×50)-grid with a mass step of 0.4 (so we explored a 20 mass range) around the guess value $m_{guess} = 28$. Then, we generated the templates using the PyCBC package and assuming the `SEOBNRv4_opt` (Spinning nonprecessing Effective One Body Numerical Relativity waveform model) approximation, translated to make it overlap the gravitational signal, and performed matched filtering for each pair of (m_1, m_2) to identify the values that produce a higher SNR. With the best values $m_{1,best}$ and $m_{2,best}$, we repeated a matched filtering operation and found the event time and the SNR value for each IFO. We removed 4 seconds at the beginning and at the end for the PSD filtering with 4 additional seconds at the beginning to account for the template length. We took the absolute value of the SNR obtained from the matched filtering process, which returns a complex quantity. The real component corresponds to the SNR associated with directly filtering the data using the template, while the imaginary component represents the SNR obtained when filtering with a template that is phase-shifted by 90 degrees. Thereafter, we scaled the template amplitude and phase to the peak value and "whiten"[2] the signal with the PSD. We applied a bandpass (30-300) Hz and isolated an asymmetric time range of 2 seconds before and 1 second after the event. Finally, we performed the Q-trasformation to catch the gravitational signal in frequency-time domain.

3 SGWB

We now consider a particular type of diffuse signal: the *Stochastic Gravitational Wave Background* (SGWB). This background arises from the superposition of gravitational waves emitted by various sources across different cosmological epochs. It is possible to distinguish between an astrophysical gravitational wave background (AGWB) and a cosmological gravitational wave background (CGWB). The latter results from various processes that occurred in the primordial universe, such as inflation, phase transitions, cosmic strings, and primordial black holes. At high redshifts, this background may have originated from the inflationary expansion of the universe, and its detection would provide a crucial tool for cosmological studies.
The unresolved sources contributing to the AGWB include compact binary systems in inspiral or merger phases, binary stars, pulsars, and supernovae.

[1] Welch's method is a spectral density estimation technique used in signal processing to estimate the power of a signal at different frequencies by dividing the data into overlapping segments and analyzing their periodograms (obtained by converting a signal from the time domain to the frequency domain).

[2] "Whitening" is a process that adjusts data to have roughly equal amounts of power at each frequency. This will tend to suppress places with high noise, and highlight places with low noise. This is helpful for finding signals, because frequencies with low noise are where the instrument is most sensitive.

A stochastic background is characterized by the fact that the amplitudes $h_P(f,\hat{\Omega})$ (where $P=+,\times$ is the polarization, $\hat{\Omega}$ is a unit vector that indicates the direction in the sky from which the GW is observed) are random variables. The analysis of a signal arising from the Stochastic Gravitational Wave Background (SGWB) proceeds under the following assumptions:

1. The SGWB is isotropic, which that signals coming from different directions are not correlated:
$$\langle h_P^*(f,\hat{\Omega}) h_P(f'\hat{\Omega}')\rangle \propto \delta^2(\Omega,\Omega') \quad . \tag{14}$$
2. The SGWB is a stationary background. This implies that the two-point correlator satisfies
$$\langle h_P^*(t,\hat{\Omega}) h_{P'}(t',\hat{\Omega}')\rangle \propto \delta(t-t') \quad . \tag{15}$$
Stationarity also means that the expectation value $\langle h(t)\rangle$ is constant and (since one is interested in the time-dependent variations of the metric) can be set to 0.
This assumption is well justified since the background is produced by astrophysical or cosmological phenomena whose characteristic timescales for significant change exceed the duration of typical observations, which span only a few years.
3. The SGWB is Gaussian. Gaussianity implies that all statistical properties of the process are fully determined by its mean and covariance. Equivalently, all higher-order correlators can be expressed as sums or products of two-point correlators and means.
4. The SGWB is unpolarized, which is a natural assumption given that it arises from the superposition of gravitational waves originating from a large number of sources.

Under these assumptions, the SGWB is statistically characterized by its power spectral density $S^P(f)$, such that

$$\langle \tilde{h}_P^*(f,\hat{\Omega}) \tilde{h}_{P'}(f',\hat{\Omega}')\rangle = \frac{1}{4\pi}\delta^2(\hat{\Omega},\hat{\Omega}')\delta(f-f')\delta_{PP'}\frac{1}{2}S^P(f)\,, \tag{16}$$

where the numerical factors arise from normalization conventions. Note that $S^P(f)$ is defined separately for each polarization mode.
The task of this experience consists in building a pipeline to generate simulated data for the SGWB with Einstein Telescope in the 2L (see Sec. 3.1) configuration and evaluate the SNR for a signal of astrophysical origin.

3.1 Einstein Telescope

The Einstein Telescope (ET) is a third-generation interferometric gravitational wave detector being developed by a collaboration of European research institutes. Construction is expected to begin the 2030s, with the first GW detections anticipated by the middle of the next decade.
Two main configurations are currently under consideration for ET: a triangular-shaped observatory (ETT), or a network of two L-shaped interferometers (ET2L) located respectively in the Netherlands (Meuse Rhine region) and Sardinia (Sos Enattos mine). In either case, each ET detector will consist of two independent optical systems: one optimized for the low-frequency band (1–10 Hz), and the other for the high-frequency band (10–10000 Hz).

3.2 SNR estimation for ET2L

3.2.1 Theoretical SNR

Our analysis focused on ET in the 2L configuration.
First of all, it is necessary to characterize the correlation between the signals detected by the two interferometers. This can be done by computing the *overlap reduction function* of the pair of detectors.
Initially, the orthonormal basis used to describe the direction of an incoming GW is defined as follows:

$$\begin{cases} \hat{m} = (\cos\theta\cos\phi,\ \cos\theta\sin\phi,\ -\sin\theta) \\ \hat{n} = (-\sin\phi,\ \cos\phi,\ 0) \\ \hat{k} = (\sin\theta\cos\phi,\ \sin\theta\sin\phi,\ \cos\theta)\,. \end{cases} \tag{17}$$

where θ, ϕ are polar coordinates on the sky surface. The polarization modes in the general orthonormal basis are

$$\begin{aligned} \tilde{e_+} &= \hat{m}\otimes\hat{m} - \hat{n}\otimes\hat{n} \\ \tilde{e_\times} &= \hat{m}\otimes\hat{n} + \hat{n}\otimes\hat{m}\,, \end{aligned} \tag{18}$$

and the *angular pattern function* is defined as

$$F^\lambda(\theta,\phi) = D^{ij}e^\lambda_{ij}(\theta,\phi)\,. \tag{19}$$

In Eq. 19, D^{ij} is the so called *detector tensor*, which contains information about the detector geometry and is defined as

$$D^{ij} = \frac{1}{2}\{u^i u^j - v^i v^j\}\,, \tag{20}$$

where u and v are the unit vectors directed along the arms of the interferometer.
We can finally write the overlap reduction function γ_{IJ} for a pair (I,J) of detectors as

$$\gamma^T_{IJ}(f) = \frac{5}{8\pi}\int d^2\hat{\Omega}\sum_{\lambda=+,\times} F^\lambda_I(f,\hat{\Omega})F^\lambda_J(f,\hat{\Omega})e^{-i2\pi f\frac{(\vec{x}_I-\vec{x}_J)\cdot\hat{\Omega}}{c}} \tag{21}$$

where $\vec{x}_I$ and $\vec{x}_J$ are position vectors of I and J respectively.
Subsequently, we tried to evaluate the SNR. The expected SNR for a cross correlation search, for an unpolarized and isotropic SGWB is provided by

$$\mathrm{SNR} = \frac{3H_0^2}{10\pi^2}\sqrt{T}\left[2\int_0^{+\infty} df \sum_i^M \sum_{j>i}^M \frac{(\gamma_{ij}(f)\Omega_{GW}(f))^2}{f^6 N_i(f) N_j(f)}\right]^{1/2} \quad . \tag{22}$$

where Ω_{GW} is the energy density spectrum of the SGWB[3], H_0 is the Hubble constant and T the observational period. Eq. 22 is valid for a stationary and non-correlated noise between the two interferometers, such that the two point correlation function for the noise components n_I, n_J is

$$\langle n_I(f) n_J^*(f')\rangle = \delta(f-f')N_{IJ}(f)\delta_{IJ} \quad . \tag{24}$$

We also assumed a *power-law* distribution for $\Omega_{GW}(f)$, which adequately describes the ASGWB:

$$\Omega_{GW}(f) = 10^{A_{gw}}\left(\frac{f}{f_{ref}}\right)^{n_{gw}} \quad , \tag{25}$$

[3] More precisely $\Omega_{GW}(f)$ is the energy density spectrum $\rho_{GW}(f)$ per logarithmic bin of frequency normalized at the critical energy density of the universe ρ_c:

$$\Omega^P_{GW}(f) = \frac{1}{\rho_c}\frac{d\rho^P_{GW}}{d\ln f} = \frac{8\pi G}{3H_0^2}\frac{dE_{GW}}{d\ln f}\,. \tag{23}$$

where we choose $n_{gw} = \frac{2}{3}$ and $A_{gw} = -9$ as testing values.
The computation of the SNR under the hypotheses mentioned in the previous sections was implemented through a Python script.

3.2.2 SNR from simulated data

Thanks to the following relation between $\Omega^P_{GW}(f)$ and $S^P(f)$

$$\Omega^P_{GW}(f) = \frac{2\pi^2}{3H_0^3} f^3 S^P(f) \quad , \tag{26}$$

one can rewrite Eq. 16 as

$$\langle h^*_I(f) h_J(f') \rangle = \frac{3H_0^2}{20\pi^2 f^3} \gamma_{IJ}(f) \Omega_{GW}(f) \delta(f - f') \, . \tag{27}$$

Given Eq. 27, 24, the expected $h(f)$ and $n(f)$ forms are computed as

$$\begin{aligned} h_I(f) &= \frac{\xi^{(h)}_{I,Re}(f) + i\xi^{(h)}_{I,Im}(f)}{\sqrt{2}} \sqrt{T_{seg} \cdot \frac{3H_0^2}{20\pi^2 f^3} \gamma_{IJ}(f) \Omega_{GW}(f)} \\ n_I(t,f) &= \frac{\xi^{(n)}_{I,Re}(t,f) + i\xi^{(n)}_{I,Im}(t,f)}{\sqrt{2}} \sqrt{\frac{T_{seg} N_d(f)}{2}} \, , \end{aligned} \tag{28}$$

where $\xi(f)$ are gaussian random variables with mean 0 and covariance 1 and the amplitudes are given by the square root of the covariances of the SGWB signal and noise respectively.
As explained in App. A.1, to simulate a SGWB's detection by ET2L, the values of $\xi(f)$ were computed using the Cholesky decomposition of the following covariance matrix:

$$\mathrm{Cov}_\xi(f) = \begin{bmatrix} 1 & \gamma_{IJ(f)} \\ \gamma_{IJ}(f) & 1 \end{bmatrix} \, . \tag{29}$$

Given the simulated signals $s(f)_I = h_I(f) + n_I(f)$, $s(f)_J = h_J(f) + n_J(f)$ for a certain observation time T, one defines

$$Y_T = \int_{-\infty}^{+\infty} df \int_{-\infty}^{+\infty} df' s^*_I(f') s_J(f) Q(f) \, . \tag{30}$$

Then, the SNR is computed as follows:

$$S_T \equiv \langle Y_T \rangle = \int_{-\infty}^{+\infty} df \int_{-\infty}^{+\infty} df' \, \langle \tilde{s}^*_I(f') \tilde{s}_J(f) \rangle \, \tilde{Q}(f) \tag{31}$$

$$N_T^2 \approx [\langle Y_T \rangle^2 - \langle Y_T^2 \rangle]_{h \approx 0} \tag{32}$$

$$\frac{S}{N} = \sqrt{\frac{\langle Y_T \rangle^2}{[\langle Y_T \rangle^2 - \langle Y_T^2 \rangle]_{h \approx 0}}} \, . \tag{33}$$

where $\tilde{Q}(f) \propto \frac{\gamma^T_{IJ}(f) \Omega_{GW}(f)}{f^3 N_I(f) N_J(f)}$ is the optimal filter function for a SGWB signal.
In practice to compute the SNR from the simulated signal for an observation time of $T = 1$ day, we considered subsequent realizations of the signal for I and J in time segments of $T_{seg} = 4$ s. Then, S_T and N_T were estimated as the average and covariance of the set of $Y_{T_{seg}}(f)$ evaluated for each T_{seg}. We chose a frequency resolution of $4/T_{seg}$ [4] and integrated in the frequency band of ET (from 1 Hz to 10^4 Hz). The steps explained above were implemented using a Python script.

[4] For computational efficiency we did not choose $1/T_{seg}$, which would have been the maximum frequency resolution possible.

4 Results

4.1 GW170814

First of all, we stated that the three interferometers were in observing mode, comparing the raw temporal series of the strain $h(t)$ with the DataQualityFlag, reported in Fig. 3. As we can see, the gravitational signal is not visible, and the signal is dominated by noise.

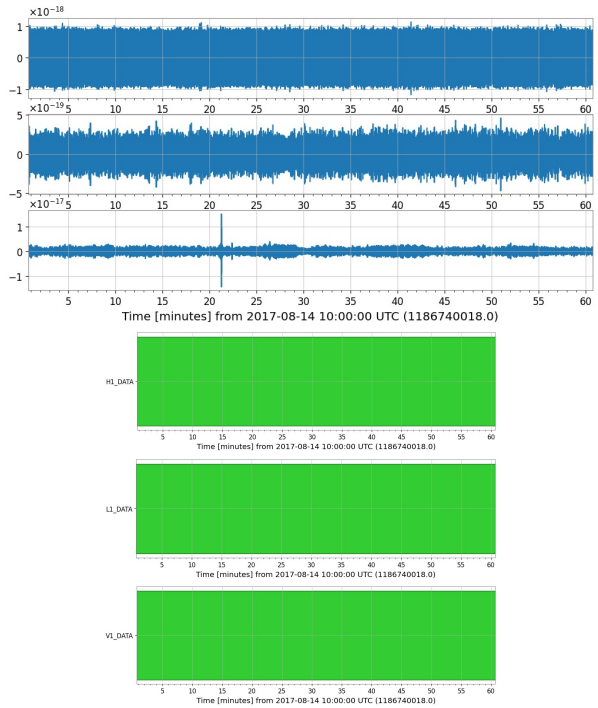

Figure 3: Raw temporal series of the strain $h(t)$ with the relative DataQualityFlag. We can see data correspond to green flags, so the interferometers are all in observing mode.

Subsequently, we plotted the ASD, selecting an interval of 4 seconds around the signal, in order to choose the frequency ranges in which the interferometers were more sensitive. The ASD curves for LIGO and VIRGO are reported in the Fig. 4. LIGO-Livingston (L1) clearly results as the most sensitive detector, while VIRGO (V1) the least sensitive. Thanks to this plot, we were able to qualitatively determine in which range of frequencies the ASD should be considered constant. We chose a bandwidth of 20 Hz and the following ranges:

- 145-165 Hz for H1;
- 145-165 Hz for L1;
- 65-85 Hz for V1.

Thereafter, in order to investigate the noise stationarity, we divided the data stream of each ASD into 180 segments of 20 seconds and computed the average and the standard deviation of the ASD values in the frequency-band previously selected. The stationarity index is provided by the ratio between standard deviation and average. These ASD values had been plotted in the histograms reported in Fig. 5, while average, standard deviation and stationarity index results are listed in Tab.1. Hanford detector was the one with the highest stationarity.

Table 1: Mean values, standard deviation and stationarity index for the ASD of each interferometer. The frequency range selected for the analysis are reported.

Parameter	**H1**	**L1**	**V1**
Frequency interval	145 - 165 Hz	145 - 165 Hz	65 - 85 Hz
ASD mean	$6.888 \times 10^{-24}\,\mathrm{Hz}^{-1/2}$	$6.977 \times 10^{-24}\,\mathrm{Hz}^{-1/2}$	$1.990 \times 10^{-23}\,\mathrm{Hz}^{-1/2}$
ASD standard deviation	$2.268 \times 10^{-25}\,\mathrm{Hz}^{-1/2}$	$2.362 \times 10^{-25}\,\mathrm{Hz}^{-1/2}$	$7.023 \times 10^{-25}\,\mathrm{Hz}^{-1/2}$
Stationarity index (std/mean)	0.033	0.034	0.035

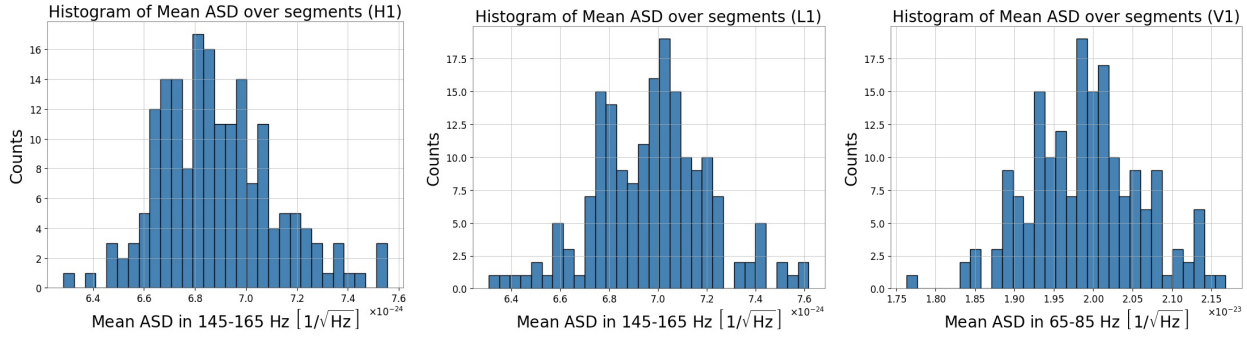

Figure 5: Histograms of the mean values of the ASD of the interferometers computed for each segments.

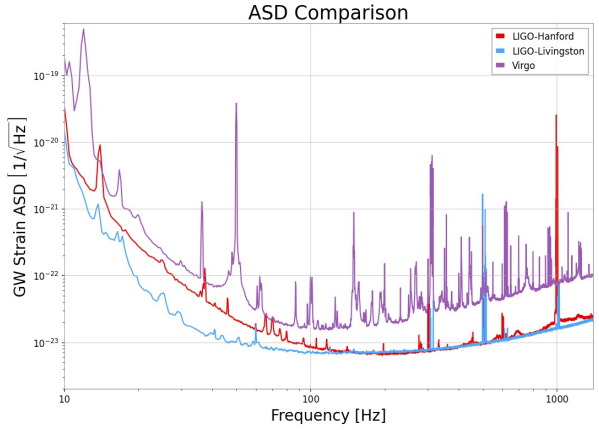

Figure 4: ASD curves of H1, L1, and V1. We can se that L1 is the most sensitive while V1 is the least one. We can observe some power lines that affected negatively the sensitivity for each instruments.

We proceeded by cleaning data and perform time domain analysis. We applied a band pass of (64-250) Hz instead of (50-300)Hz in order to avoid the power lines, visible in the ASD plot (Fig.4), at 50 Hz (V1), 60 Hz (H1 and L1) and ∼300 Hz (H1, L1 and V1). In the subsequent step, we plotted cleaned time series, that are reported in Fig. 6. Gravitational signal still not appear as visible and the noise dominates.

Then, we searched for the optimal filter as explained in Sec. 2. We plotted the distribution of SNR in a (m_1, m_2)-grid for each detector and computed the maximum SNR value and its location in the grid. The results are reported in Fig. 7 and listed in Tab. 2, where are compared with the results from the article [2]. We associated the resolution used to scan the mass values around m_{guess} as the uncertainty on $m_{1,best}$ and $m_{2,best}$.

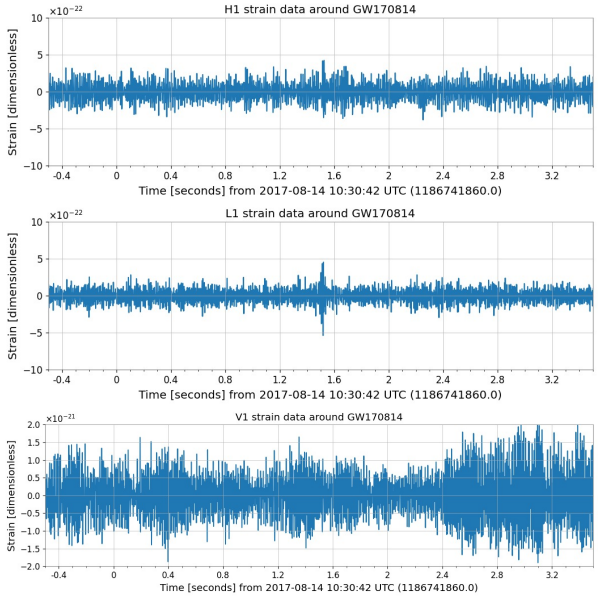

Figure 6: Time series of the strain after bandpass. We plotted a 4 seconds time window around t_0. The gravitational signal is still not visible.

The first detector to reveal the signal was Livingston, followed by Hanford with a delay of ∼9 ms and finally by Virgo after ∼13 ms.These values are in agreement with the ones reported in [2], which are ∼8 ms and ∼14 ms, respectively.

Finally, we whitened the signal obtaining the gravitational signal and comparing it with the model. We performed the Q-trasformation to catch the gravitational signal in frequency-time domain. The results for each interferometer are reported in Fig. 8 along with the SNR.

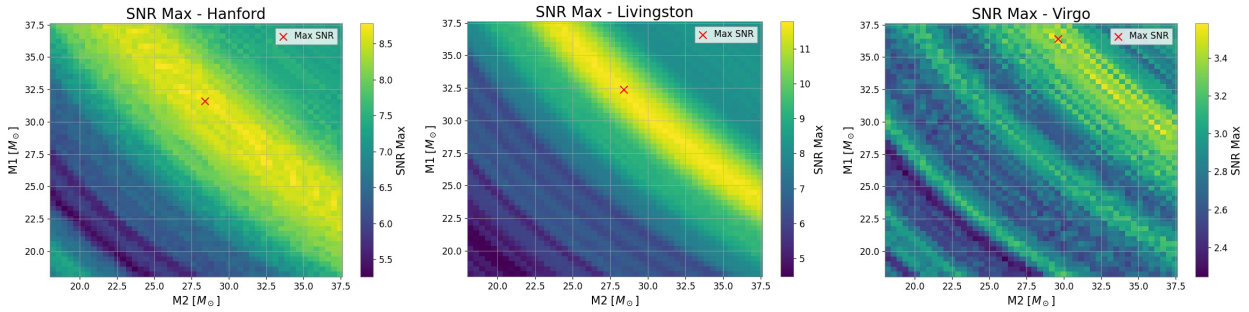

Figure 7: Distribution of the SNR values in the (m_1, m_2)-grid. The maximum SNR position is represented by the red cross.

Table 2: Best values for m_1 and m_2 and SNR values computed for each detectors. The values indicated with (*) are the ones reported in [2]. The masses (*) are refered to the source frame. The times are computed from the gps time $t = 1186741861$ s.

Parameters	**Hanford**	**Livingston**	**Virgo**	**Best-value***
$m_{1,best}$ $[M_\odot]$	31.6±0.4	32.4±0.4	36.4±0.4	$30.5^{+5.7}_{-3.0}$
$m_{1,best}$ $[M_\odot]$	28.4±0.4	28.4±0.4	29.4±0.4	$25.3^{+2.8}_{-4.2}$
SNR	8.8	11.8	3.6	—
SNR*	7.3	13.7	4.4	—
Event Time Detection [s]	0.53	0.52	0.54	—

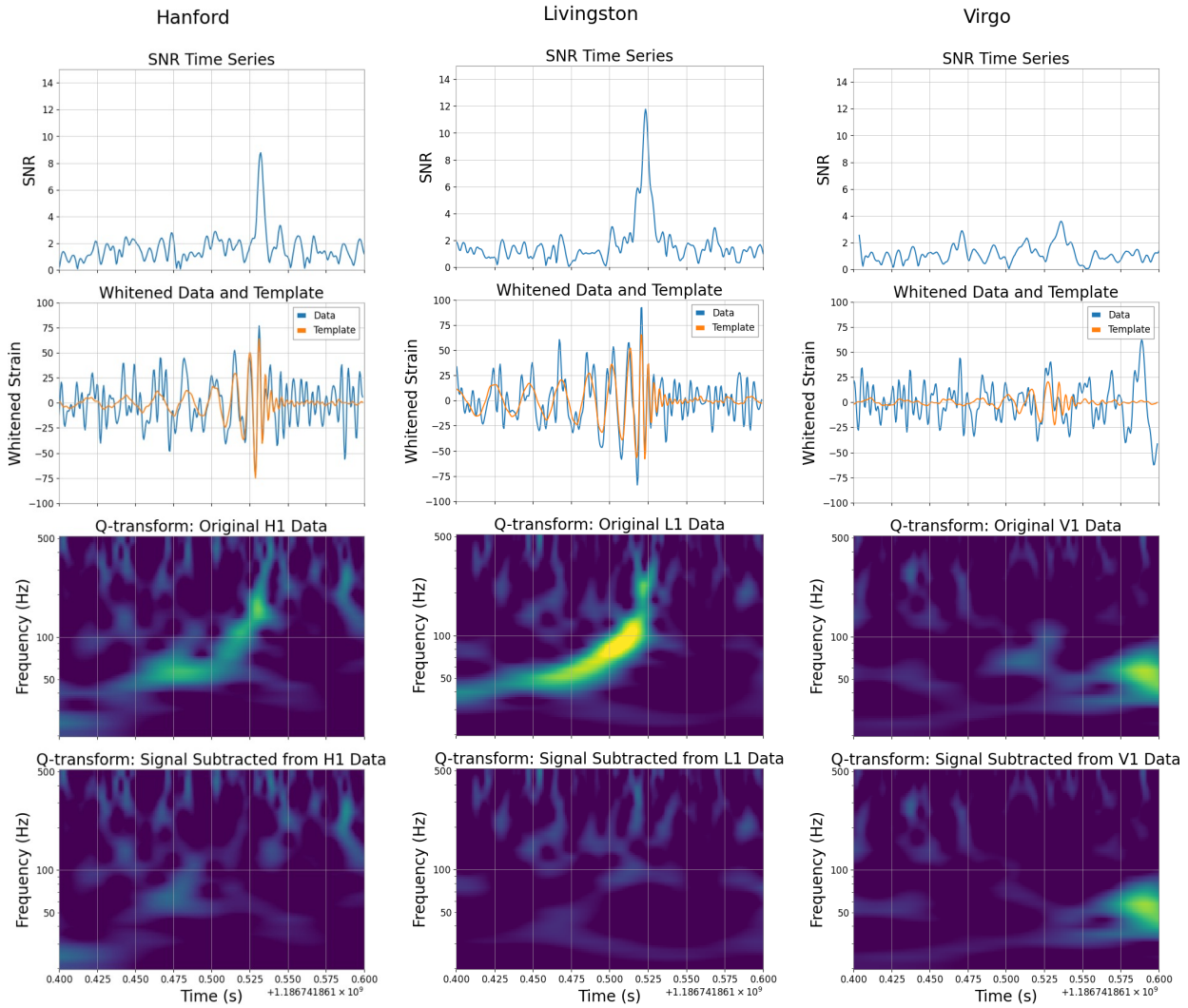

Figure 8: The GW event GW170814 observed by LIGO Hanford, LIGO Livingston, and Virgo on August 14, 2017, 10:30:43 UTC. *Top row:* SNR time series. It is possible to observe a peak corresponding to the GW signal in both Hanford and Livingston. As expected from the results obtained (see Tab. 2), the peak in Virgo is not clearly distinguishable from noise. *Second row:* time series of the whitened strain. The signal is reported in blue while the template is reported in orange. Again, we can observe that the noise component is strong in Virgo. *Bottom rows:* representation of the signal in the time-frequencies domain. In second panels the signal was subtracted to highlight the noise. A glitch in Virgo is visible at ∼0.575 s.

4.2 SGWB

The theoretical SNR for ET2L was evaluated for 2 different configurations. The first configuration consists of two detectors with parallel arms [5], while in the second one the corresponding arms are rotated by 45°. One of those realizations for the aligned and misaligned case are shown in Fig. 9, 10 respectively.

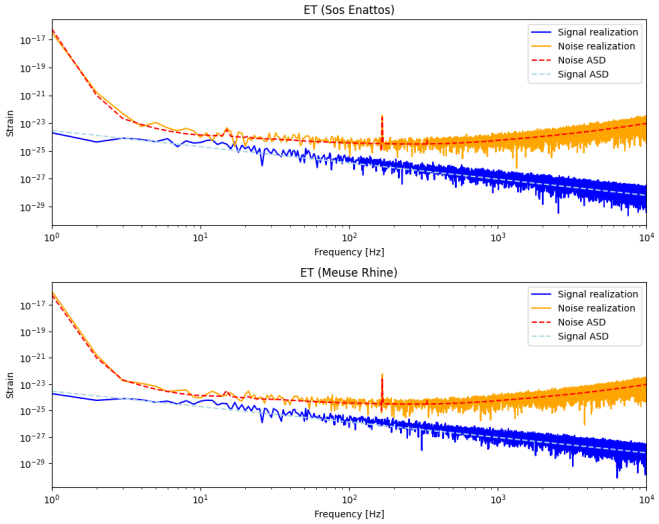

Figure 9: Noise and signal realization for ET2L in the aligned configuration. For reference we also plotted the ASD for the signal and the noise.

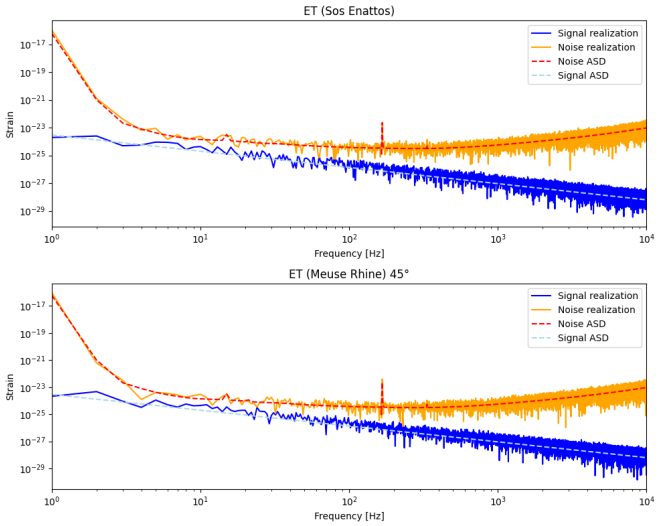

Figure 10: Noise and signal realization for ET2L in the misaligned configuration.

For the same configurations, we also computed the SNR value for the simulated SGWB signals as previously explained. The results of our analysis are shown Tab. 3.

Table 3: Theoretical and simulated SNR values for ET2L in the aligned and misaligned configuration.

Configuration	SNR theoretical	SNR simulated
ET2L aligned	55.5	26.4
ET2L 45°	0.13	0.52

[5] More specifically we considered the case where both detectors have one arm pointing North and the other pointing East.

5 Discussion

5.1 GW170814

The stationarity index allowed us to identify which detector has the most stationary noise. Analyzing the ratio between the standard deviation and the mean of the ASD provides insight into whether the power within the frequency band varies significantly over time. For stationary noise, these means should remain approximately constant, resulting in a narrow distribution centered around a fixed value. Conversely, if the noise is non-stationary, the means fluctuate, leading to a broader distribution. Therefore, if the standard deviation of the segment means is small compared to the overall mean, the noise can be considered stable; if it is large, the noise is variable. Although the values are all quite close, Hanford exhibits a smaller standard deviation relative to the others, indicating more stable noise (see Tab. 1).

Thanks to the ASD plot, we were also able to apply a bandpass filter that allowed us to avoid the typical power line noise observed in LIGO and Virgo data and to restrict to the most sensitive region. However, this procedure did not allow us to isolate the gravitational signal effectively. Nonetheless, a more detailed analysis, employing matched filtering and signal whitening, enabled us to identify the presence of a gravitational wave.

The analysis of the SNR for different combinations of masses around the central value allowed us to determine the best-fit values $m_{1,\mathrm{best}}$ and $m_{2,\mathrm{best}}$ for the initial black hole masses that generated the signal. In order to compare our mass estimates with the results presented in [2], it is important to note that the masses reported in that work refer to the source frame. Therefore, to obtain the detector-frame masses and ensure a consistent comparison, we must multiply the source-frame values by the factor $(1+z)$. According to [2], the redshift is $z = 0.11^{+0.03}_{-0.04}$, resulting in observer-frame masses of approximately $m_1 \sim 33.9\,M_\odot$ and $m_2 \sim 28.1\,M_\odot$. Thanks to this adjustment, our estimated values are consistent with those reported in the article within the uncertainties. The values obtained for the Hanford and Livingston detectors are mutually compatible, while the result from Virgo is not. Furthermore, the high values of the component masses support the hypothesis that the observed signal was produced by the coalescence of two black holes, in agreement with expectations based on the initial gravitational-wave event catalog.

During the mass estimation, we encountered several difficulties in analyzing the Virgo data. Using the same parameters adopted for LIGO, we obtained two mass values ($m_{1,\mathrm{best}} \sim 28.4\,M_\odot$ and $m_{2,\mathrm{best}} \sim 23.2\,M_\odot$) that were not consistent with those derived from LIGO. In addition, the time delay between the detection of the gravitational wave with respect to Livingston was found to be approximately 100 ms, which is significantly larger than the light travel time between L1 and V1. We attributed these inconsistencies to the higher noise level affecting Virgo compared to LIGO. To mitigate this issue, we repeated the analysis by restricting the data to a 49 ms time window around the event time measured by L1, in order to avoid glitches. Indeed, according to [2], a noise transient with a central frequency around 50 Hz occurs in the Virgo detec-

tor ∼50 ms after GW170814. This transient lies outside the time window expected from the light travel time between the detectors and therefore has no impact on the interpretation of the GW signal. This procedure allowed us to obtain mass values for Virgo that are closer to those found for LIGO, and a detection time consistent with the results reported in [2].

The position of the signal is consistent across all the plots (the SNR, the whitened strain, and the time series) reported in Fig. 8). However, we observe the presence of a signal at ∼0.575 s in the Virgo data, which is attributable to transient noise. Nonetheless, the matched filtering procedure successfully identified the GW signal, as evidenced by its correspondence with the peak in the SNR plot. Consistent with the values reported in Table 2, the detector with the highest SNR is Livingston, while Virgo has the lowest, reflecting its higher noise level.

Finally, we note that during our analysis it was not developed a fully satisfactory treatment of the uncertainties associated with the measurements. As a result, the uncertainties reported for the best mass values are almost certainly underestimated. For a more accurate assessment, a Bayesian analysis of confidence intervals and credible regions would be necessary.

5.2 SGWB

The results in Tab. 3 demonstrate the capability of Einstein Telescope to detect the ASGWB, whose energy spectrum is well described by the adopted power-law model. The SNR value obtained from the simulated data is slightly different than the theoretical expectation, as predictable. The discrepancy is caused by the numerical approximation necessary to compute both quantities. Indeed by lowering the frequency resolution (up to a minimum of $1/T_{seg}$) for the simulated data, one could obtain significantly higher SNR values but with longer computational time and memory usage. However, the order of magnitude of the estimates always remain roughly the same.
Given the computed SNR for both configurations of ET2L, it is clear that the aligned one will be more sensitive to the background signal. To reach the same SNR, the misaligned ET2L would need a much longer observational time. Fig. 11, 12 shows the overlap reduction functions for the two detectors couple. The one for the misaligned case remains consistently lower than 0.05, resulting in lower values for the SNR when computing the integrals in Eq. 30 - 33.

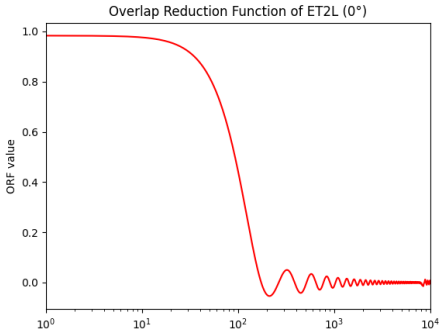

Figure 11: Overlap reduction function for ET2L in the aligned configuration. The "glitch" in the oscillations near the 10^4 Hz mark is only due to numerical computation.

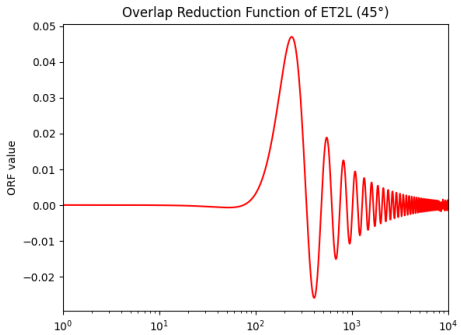

Figure 12: Overlap reduction function for ET2L in the misaligned configuration.

Current interferometers are not yet capable of detecting the SGWB, but we can expect great improvements from the third generation GWs detectors like ET. It is worth noting that the observation time can extend well beyond a single day, up to the order of several years, which could potentially allow for the detection of even the cosmological components of the background.

6 Conclusion

On August 14, 2017, the LIGO and Virgo interferometers observed a gravitational-wave signal originating from the merger of two stellar-mass black holes. We found that the signal was first detected at LIGO Livingston, followed by Hanford and Virgo with delays of ∼9 ms and ∼13 ms, respectively. The signal analysis yielded SNR values of ∼8.8 for the Hanford detector, ∼11.8 for Livingston, and ∼3.6 for Virgo. The estimated original masses of the two black holes were found to be $(m_1, m_2) = (31.6 \pm 0.4, 28.4 \pm 0.4)\, M_\odot$ for Hanford, $(32.4 \pm 0.4, 28.4 \pm 0.4)\, M_\odot$ for Livingston, and $(36.4 \pm 0.4, 29.4 \pm 0.4)\, M_\odot$ for Virgo.

Finally, The SNR achievable by Einstein Telescope in the 2L configuration for a SGWB signal was computed. The SNR value obtained from the simulated data are 26.4 for aligned and 0.52 for misaligned setups.

A Appendix

A.1 Cholesky matrix

The following concepts were found in [6], p.3. Given a certain covariance matrix Σ this can be uniquely factorized as $\Sigma = L^T L$, where L is a superior triangular matrix with positive elements on the diagonal, namely a Cholesky matrix. In the case of a SGWB simulated signal (see Eq. 28) we know the covariance matrix between the variable $\xi_I(f)$ e $\xi_J(f)$:

$$\mathrm{cov}_\xi(f) = \begin{bmatrix} 1 & \gamma_{IJ}(f) \\ \gamma_{IJ}(f) & 1 \end{bmatrix} \tag{34}$$

where $\gamma_{IJ}(f)$ is the overlap reduction function for I and J. If we now define four gaussian variables $\xi_I^{Re}(f)$, $\xi_I^{Im}(f)$, $\xi_J^{Re}(f)$, and $\xi_J^{Im}(f)$ with mean 0 and variance equal to 1, then by computing

$$\begin{bmatrix} \xi_I(f) \\ \xi_J(f) \end{bmatrix} = \frac{1}{\sqrt{2}} \left(L \begin{bmatrix} \xi_I^{Re}(f) \\ \xi_J^{Re}(f) \end{bmatrix} + iL \begin{bmatrix} \xi_I^{Im}(f) \\ \xi_J^{Im}(f) \end{bmatrix} \right) \tag{35}$$

we can generate two complex gaussian variables $\xi_I(f)$ e $\xi_J(f)$ with a covariance matrix equal to

$$\begin{aligned}\mathrm{cov}_{IJ}(f) &= \frac{1}{2}\left(L\,\mathrm{cov}_{Re}(f)\,L^T + L\,\mathrm{cov}_{Im}(f)\,L^T\right)\\ &= \frac{1}{2}(2\,L^T\,L) = \mathrm{cov}_\xi(f) \quad \Rightarrow\\ &\mathrm{cov}_{IJ}(f) = \mathrm{cov}_\xi(f)\,. \end{aligned} \tag{36}$$

This was used to compute $h(f)$ and $n(f)$ in Eq. 28.

References

[1] URL: https://gwosc.org/.

[2] B. P. Abbott et al. "GW170814: A Three-Detector Observation of Gravitational Waves from a Binary Black Hole Coalescence". In: *Phys. Rev. Lett.* 119.14 (2017), p. 141101. DOI: 10.1103/PhysRevLett.119.141101. arXiv: 1709.09660 [gr-qc].

[3] B. P. Abbott et al. "GWTC-1: A Gravitational-Wave Transient Catalog of Compact Binary Mergers Observed by LIGO and Virgo during the First and Second Observing Runs". In: *Phys. Rev. X* 9.3 (2019), p. 031040. DOI: 10.1103/PhysRevX.9.031040. arXiv: 1811.12907 [gr-qc].

[4] Loris Amalberti, Nicola Bartolo, and Angelo Ricciardone. "Sensitivity of third-generation interferometers to extra polarizations in the stochastic gravitational wave background". In: *Physical Review D* 105.6 (Mar. 2022). ISSN: 2470-0029. DOI: 10.1103/physrevd.105.064033. URL: http://dx.doi.org/10.1103/PhysRevD.105.064033.

[5] M. Branchesi et al. "Science with the Einstein Telescope: a comparison of different designs". In: *Journal of Cosmology and Astroparticle Physics* 07 (2023), p. 068. DOI: 10.1088/1475-7516/2023/07/068. eprint: 2303.15923.

[6] Thomas Muschinski et al. "Cholesky-based multivariate Gaussian regression". In: *Econometrics and Statistics* 29 (Jan. 2024), pp. 261–281. ISSN: 2452-3062. DOI: 10.1016/j.ecosta.2022.03.001. URL: http://dx.doi.org/10.1016/j.ecosta.2022.03.001.